PAPER

Atomic-layered V₂C MXene containing bismuth elements: 2D/0D and 2D/2D nanoarchitectonics for hydrogen evolution and nitrogen reduction reaction†

Sana Akir, [ID] * Jalal Azadmanjiri, Nikolas Antonatos, [ID] Lukáš Děkanovský, Pradip Kumar Roy, Vlastimil Mazánek, Roussin Lontio Fomekong, Jakub Regner and Zdeněk Sofer [ID] *

The exploitation of two-dimensional (2D) vanadium carbide (V_2CT_x, denoted as V_2C) in electrocatalytic hydrogen evolution reaction (HER) and nitrogen reduction reaction (NRR) is still in the stage of theoretical study with limited experimental exploration. Here, we present the experimental studies of V_2C MXene-based materials containing two different bismuth compounds to confirm the possibility of using V_2C as a potential electrocatalyst for HER and NRR. In this context, for the first time, we employed two different methods to synthesize 2D/0D and 2D/2D nanostructures. The 2D/2D V_2C/BVO consisted of $BiVO_4$ (denoted BVO) nanosheets wrapped in layers of V_2C which were synthesized by a facile hydrothermal method, whereas the 2D/0D V_2C/Bi consisted of spherical particles of Bi (Bi NPs) anchored on V_2C MXenes using the solid-state annealing method. The resultant V_2C/BVO catalyst was proven to be beneficial for HER in 0.5 M H_2SO_4 compared to pristine V_2C. We demonstrated that the 2D/2D V_2C/BVO structure can favor the higher specific surface area, exposure of more accessible catalytic active sites, and promote electron transfer which can be responsible for optimizing the HER activity. Moreover, V_2C/BVO has superior stability in an acidic environment. Whilst we observed that the 2D/0D V_2C/Bi could be highly efficient for electrocatalytic NRR purposes. Our results show that the ammonia (NH_3) production and faradaic efficiency (FE) of V_2C/Bi can reach 88.6 µg h^{-1} cm^{-2} and 8% at −0.5 V *vs.* RHE, respectively. Also V_2C/Bi exhibited excellent long-term stability. These achievements present a high performance in terms of the highest generated NH_3 compared to recent investigations of MXenes-based electrocatalysts. Such excellent NRR of V_2C/Bi activity can be attributed to the effective suppression of HER which is the main competitive reaction of the NRR.

1. Introduction

Currently, fossil fuels supply about 80% of the world's energy consumption.[1] However, fossil fuel stocks are limited, and their intensive use will aggravate the problems of greenhouse gas emissions. Therefore, there is an urgent need to increase the utilization of renewable energy resources to meet our ever-increasing energy demands. Hydrogen gas (H_2), and ammonia (NH_3) are among the most produced and widely used chemicals in the world.[2,3] Therefore, the production of NH_3 and H_2 through an economic and sustainable process is highly sought

after. The electrochemical hydrogen evolution reaction (HER), and nitrogen reduction reaction (NRR) have attracted widespread attention owing to fossil-fuel-free routes for H_2 and NH_3 synthesis, respectively. To date, precious metals are the most outstanding electrocatalysts for electrochemical H_2 and NH_3 production, especially platinum-based nanomaterials for HER,[4] and palladium-based nanomaterials for NRR.[5] However, the high cost of those precious metals is restricting their practical applications. Therefore, it is urgent to find economical and effective NRR and HER electrocatalysts. Two-dimensional (2D) transition-metal carbides, nitrides, and carbonitrides (MXenes) have received great interest since the discovery of the first MXene ($Ti_3C_2T_x$).[6] MXenes usually have a hexagonal close-packed structure with a chemical formula of $M_{n+1}X_n$ (M = transition metal element, X = C, N, n = 1–3). Commonly, MXenes are obtained by selectively etching the "A" elements from their corresponding bulk MAX phases using chemicals, such as

Department of Inorganic Chemistry, University of Chemistry and Technology Prague, Technická 5, 166 28 Prague 6, Czech Republic. E-mail: akirs@vscht.cz, zdenek.sofer@vscht.cz

hydrofluoric acid, ammonium bifluoride, or an acidic solution of fluoride salts. Thus, their surfaces are inevitably terminated by a series of functional groups (–OH, –F, –O).[6] Owing to the existence of surface terminations, most MXenes exhibit both metallic conductivity and hydrophilicity,[7] which makes them promising candidates for various applications, such as energy storage and conversion, especially in electrocatalysis.[8,9] Unfortunately, the NRR and HER performances with the most developed MXenes electrocatalysts are still far from satisfactory and not comparable to those of precious metals. Most of the pristine MXenes suffer from large overpotential and low stability in aqueous electrolytes which seriously hinder their large-scale practical applications.[10,11] Additionally, MXenes often exhibit low ammonia yield and unsatisfactory faradaic efficiency (FE),[12,13] because they are usually terminated with inactive functional groups (–F, –OH), which hinder the active metal sites for N_2 binding.[14,15] Therefore, many attempts have been made to improve the HER and NRR activities of MXenes. Firstly, by introducing or modifying chemical functional groups on its surface.[16–18] It was proved that the electrocatalytic performances of MXenes are significantly influenced by the functional groups on the basal plane (–O, –OH, –F). For instance, MXenes terminated with O species presented relatively low hydrogen adsorption free energy (ΔG_{H^*}) and would be promising candidates for HER.[11] Secondly, constructing composites of MXenes with other active components (e.g., nanoparticles, oxides, single atoms, and other 2D materials) is another efficient strategy to boost the NRR and HER performance of such 2D layered structures.[19–22] In fact, the MXene-based composites could enhance the catalytic activity by increasing specific surface area (SSA). Among MXene-based composites, 2D/2D heterostructures have been identified as the best choice to ensure the largest contact area and promote electron transfer for improving electrocatalysis reactions.[23]

Recently, Bi-based catalysts have been considered potential NRR candidates owing to their intrinsic catalytic activity, earth-abundance, low cost, and environmentally benign semimetal.[24] The density functional theory (DFT) calculation also has proved that in Bi-based catalysts, the density state near the Fermi level is mainly localized around the Bi atoms, indicating the ability of Bi to serve as active sites to donate p-electrons and thus activate N_2.[25] Currently, promising advances have been achieved for the NRR on Bi-based electrocatalysts including Bi nanosheets,[24] 2D mosaic Bi nanosheets,[25] PdBi$_2$ nanoflakes,[26] and bismuthene nanostructures.[27] However, the NRR performance of the reported Bi-based materials is still limited due to their poor electrical conductivity.[25] Thus, combining Bi with conductive nanomaterials is considered a promising strategy to solve this issue. Very recently, Liu et al.,[28] successfully anchored metallic Bi on the 2D $Ti_3C_2T_x$ MXene via a simple liquid phase reduction method. The as-prepared Bi@Ti$_3$C$_2$T$_x$ composite electrocatalyst achieved an excellent NH_3 yield of 28.3 μg h^{-1} cm^{-2} and a large FE of 27.2% at 0.4 V vs. RHE. Their report shows a significant performance for NRR which is higher than most of the reported Bi-based catalysts. On the other hand, Bi-based catalysts possess poor activity in HER due to the unfavorable free energy of hydrogen adsorption (ΔG_{H^*}).[29] Thus, a lot of studies have been applied to explore the (photo) catalytic activity of H_2 production for Bi-based materials. Recently, by adopting different strategies, BiOX, (X = Cl, Br, and I),[30] Bi_2O_3,[31] and $BiVO_4$[32] showed extraordinary HER performance. Among Bi compounds, $BiVO_4$ has emerged as the most promising candidate for photocatalytic hydrogen production owing to good chemical stability, nontoxicity, and low cost.[32]

In this work, for the first time, we successfully synthesized two different MXene-based nanocomposites including V$_2$C/BVO and V$_2$C/Bi NPs. V$_2$C MXene was selected because of its high electrical conductivity compared to the other reported MXenes.[6] Our findings demonstrate that the first nanocomposite (V$_2$C/BVO) consists of $BiVO_4$ nanosheets embedded in the few layers of V$_2$C nanosheets, and the second nanocomposite (V$_2$C/Bi) consists of metallic Bi NPs anchored on the surface of V$_2$C. The V$_2$C MXene was obtained through the etching of V$_2$AlC by HCl/NaF. The as-obtained nanocomposites were directly used as multifunctional electrodes for HER and NRR in acidic and in basic electrolytes, respectively. 2D/2D V$_2$C/BVO showed a lower overpotential (384 mV) in 0.5 M H$_2$SO$_4$ aqueous electrolyte compared to pristine V$_2$C (823 mV) when applied for HER. Also, V$_2$C/BVO proved excellent stability for HER application. Meantime, V$_2$C/Bi has been proven to be highly efficient NRR electrocatalyst achieving a record high-yield rate of NH_3 production with 88.6 μg h^{-1} cm^{-2} and FE of 8% at −0.5 V vs. RHE. These results indicate that the decoration of a suitable matrix with Bi atoms is beneficial to improve nitrogen fixation performance. To the best of our knowledge, the HER and NRR electrocatalysis performances of the V$_2$C/Bi and V$_2$C/BVO have not been studied before.

2. Results and discussion

2.1. Characterization of the catalysts

The crystalline structure of V$_2$AlC, V$_2$C, and composite samples was examined by XRD as shown in Fig. 1a. Firstly, it should be
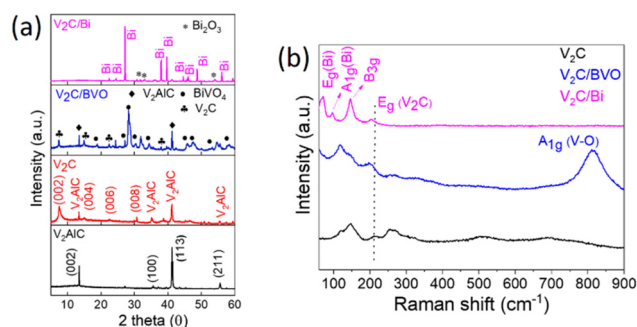

Fig. 1 (a) XRD patterns of V$_2$AlC, V$_2$C, V$_2$C/BVO, and V$_2$C/Bi. (b) Raman spectra of V$_2$C, V$_2$C/BVO, and V$_2$C/Bi.

mentioned that the as-prepared V_2AlC precursor presents sharp and strong diffraction peaks at $2\theta = 13.5°$ and $41.2°$, indicating its high crystallinity and purity (PDF file 29-0101).[33] After etching with HCl/NaF solution, several peaks were detected at 7.5°, 15°, 22.6°, and 30.7° corresponding to the crystal indexes (002), (004), (006), and (008) of hexagonal V_2C MXene with a multilayered structure.[33] The presence of small peaks observed at 13.5° and 41.2° suggests the existence of a small amount of unreacted V_2AlC, indicating the incomplete etching of V_2C. This observation is consistent with previous studies.[34,35] The same peaks were also detected in V_2C/BVO, composite confirming the unaltered hexagonal crystalline phase of V_2C in the V_2C/BVO. Additional diffraction peaks at $2\theta = 18.6°, 28.6°, 30.7°, 34.3°, 39.9°, 42.5°, 47.2$ correspond to the (011), (121), (040), (200), (211), (051) and (042), and (310), respectively, confirming the formation of monoclinic $BiVO_4$ (JCPDS no. 14-0688).[36] As well, the XRD pattern of V_2C/Bi shows that all the diffraction peaks can be indexed to Bi rhombohedral crystal structure NPs (code: 01-085-1330).[37] At the same time, the peaks originating from V_2AlC and V_2C MXene completely vanished. This can be attributed to the presence of high-density Bi nanoparticles that are fully occupied on the surface of the V_2C. As a result, it becomes difficult to detect the V_2AlC and V_2C peaks. This phenomenon has been observed in previous reports of MXene-based nanocomposites, where the (002) peak of MXenes disappeared after being combined with other components.[38–40] The loss of the (002) peak of V_2C was attributed to the relatively poor crystallinity of V_2CT_x and the low signal-to-noise ratio.[39] Low-intensity peaks of Bi_2O_3 can also be observed corresponding to surface oxidation.

The as-prepared samples were further studied by Raman spectroscopy (Fig. 1b). For V_2C, several bands appeared at approximately 147, 211, 262, 513, and 691 cm^{-1}. According to the theoretical study of Champagne *et al.*,[41] the peak at 211 cm^{-1} corresponds to the E_g mode of $V_2C(OH)_2$, the peak at 262 cm^{-1} corresponds to the E_g mode of V_2C, and two weaker peaks at 513 and 691 cm^{-1} can be assigned the A_{1g} mode of V_2CF_2 and $V_2CO(OH)$, respectively. The E_g mode is due to the in-plane vibration of the V atoms while the A_{1g} mode is due to the out-of-plane vibration of the V atoms. As well, for V_2C/BVO the typical Raman bands of V_2C are observed with slight blue-shifting, which confirms the interface interaction between $BiVO_4$ and V_2C. Other peaks at around 814, 326, and 118 cm^{-1} were also detected. The most intense Raman peak at about 814 cm^{-1} is assigned to the symmetric V–O stretching vibrations (A_{1g}), the sharp bond at 118 cm^{-1} due to external modes rotation/translation, whereas the weak band is attributed to asymmetric bending vibration (B_g) of the VO_4^{3-} group in $BiVO_4$.[42,43] The above results further prove the successful synthesis of the V_2C/BVO composite. For the second V_2C/Bi composite, three obvious peaks at 71, 97, and 146 cm^{-1} are observed. The modes located at 71 and 97 cm^{-1} can be assigned to the first-order E_g and A_{1g} stretching modes, respectively, of the Bi–Bi vibrational modes of rhombohedral Bi NPs.[27,44] The peak at 206 cm^{-1} is assigned to E_g of V_2C

$(OH)_2$ with slight blue-shift from that of pure V_2C reveals the interaction between Bi NPs and V_2C, and the predominant band at 145 cm^{-1} is attributed to the skeleton bent vibrational mode (B_{3g}), characteristic of the orthorhombic phase of V_2O_5,[45] implying the partial oxidation of the V_2C MXene. The obtained XRD and Raman results confirm the synthesis of a new composite V_2C/Bi through the reduction of Bi^{5+} in $NaBiO_3$ to metallic Bi NPs. MXene was used as a reducing agent to donate electrons and convert $NaBiO_3$ to Bi NPs. Previous research has shown that the surface termination groups of MXenes, such as –O, –OH, and –F, provide excellent adsorption and reduction properties.[46] The reduction of Bi^{5+} to Bi^0 during the synthesis of V_2C/Bi composites occurred through a reduction process involving oxidation states of +5, +3, and 0. The presence of Bi_2O_3 trace in the XRD spectrum of the V_2C/Bi composite confirmed the reduction of Bi^{5+} to Bi^{3+}. Consequently, Bi NPs are homogeneously distributed on the surface of V_2C nanosheets, which are partially oxidized during the synthesis reaction.

The investigation of the V_2C and V_2C/Bi elemental composition by EDS is displayed in Fig. S1.† The presence of V and C confirms the successful synthesis of MXene, and the existence of O, F, Cl, and Na further proves the presence of active groups on the surface of MXene. In addition, the peak corresponding to Bi in composites demonstrates the successful introduction of Bi into V_2C and the formation of a hybrid. More information about the morphology and crystal structure of the material structure was evaluated by SEM, TEM, HRTEM, and selected-area electron diffraction (SAED).

As shown in Fig. 2a, the SEM of V_2C shows the typical accordion-like multilayer nanostructure. The high-resolution TEM (HRTEM) image in Fig. S2a† reveals the crystalline lattice of V_2C MXene with an interplanar distance of 0.93 nm, corresponding to its (002) planes, indicating the well-crystallized feature of the as-synthesized V_2C MXene. The SAED pattern (inset of Fig. S2a†) reveals a hexagonal structure for V_2C which is in good agreement with the structure determined from the XRD result. As well, for V_2C/BVO, it can be observed that $BiVO_4$ flakes were uniformly wrapped on the sheet of V_2C (Fig. 2b). The TEM image in Fig. 2d further suggests that the V_2C/BVO is constituted of 2D ultrathin nanosheets. A closer observation (HRTEM in Fig. 2e) revealed the presence of intimate contact and a distinguished contrast between $BiVO_4$ and V_2C. Additionally, the interplanar distance of 0.31 and 0.93 nm can be assigned to the (121) $BiVO_4$,[47] and (002) planes of V_2C, respectively. This observation further corroborates that the as-prepared V_2C/BVO is a 2D/2D composite with intimate coupling. This junction can increase the contact area between the two materials which can enhance the electron transfer, and as a result, improve the catalytic activity.[32] In addition, the elemental mapping of V_2C/BVO (Fig. 2f) reveals the existence of homogeneous distribution of C, V, O, and Bi elements.

The selected area diffraction (SAED) image in Fig. S2b† confirms the preservation of the original hexagonal structure of MXene. For V_2C/Bi, SEM, and TEM/HRTEM images (Fig. 2c, g, and h) reveal the layered structure of V_2C was well maintained
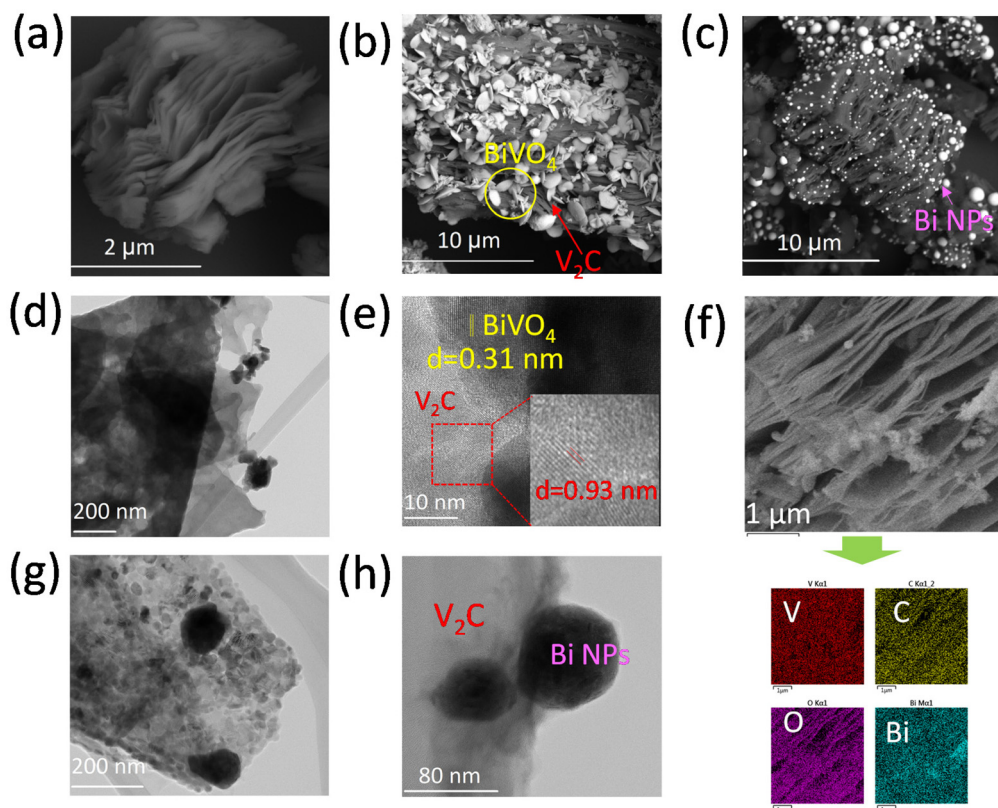
Fig. 2 SEM of (a) V_2C, (b) V_2C/BVO and (c) V_2C/Bi, (d) TEM of V_2C/BVO, (e) HRTEM of V_2C/BVO, (f) the main elemental components mapping of V, C, O and Bi of V_2C/BVO, (g) TEM of V_2C/Bi and (h) HRTEM of V_2C/Bi.

and Bi nanoparticles were loaded on the surface of the V_2C MXene. The elemental mapping results in Fig. S2c† further present the uniform distribution of V, C, Bi, and O elements, suggesting that Bi NPs are well dispersed on V_2C.

To examine the surface chemical state, the XPS of the samples was measured. Individual bonding states can exhibit slight variability in their position due to an inhomogeneous surface charging. Fig. S3a† shows the XPS survey spectra which confirmed the presence of O, V, F, and C in all three samples. Compared to the original V_2C, the decrease of the F 1s peak and enhancement of the O 1s peak of composites may be due to the substitution of –F groups by –OH groups. The detection of the Bi 4f peak confirms the construction of V_2C/BVO and V_2C/Bi heterostructures. The XPS spectrum of C 1s in V_2C (Fig. 3a) shows the presence of the main peak of C–V (282 eV) belonging to V_2C.[48] The peaks of adventitious carbon (284.4 eV), C–O (285.9 eV), C=O (287.6 eV), and O–C=O (289 eV) originate from adsorbed species on the surface of the material and from functional groups on the surface of MXene.[38,49–51] For V_2C/BVO, the peak from carbide V–C (282.6 eV) was still detected (Fig. 3b), indicating the presence of V_2C on the surface of the material. However, in the case of V_2C/Bi, the C–V bond peak disappeared (Fig. 3c), implying that the surface of MXene was highly covered with metallic bismuth. The V 2p spectrum (Fig. 3d) shows the characteristic peaks of V^{2+} species in V_2C at 513.5

$(2p_{3/2})$ and 521.4 $(2p_{1/2})$ eV, as well as V^{4+} species in V_2C at 516.5 $(2p_{3/2})$ and 524.2 $(2p_{1/2})$ eV.[48] The obvious peak (V^{2+}) confirms the strong metal carbide interaction (V–C) in V_2C, while peaks of V^{4+} confirm the existence of vanadium oxide (V–O) on the surface of V_2C. Simultaneously, the XPS spectrum of V 2p in V_2C/BVO and V_2C/Bi composites is shown in Fig. 3e and f. For both composites, the peak related to V^{2+} species can still be observed but is greatly decreased. Meanwhile, the peak intensity of V–O species increased, which proved the partial oxidation of the surface V atoms during the composite's preparations. Bi 4f peaks (Fig. S3b†) are deconvoluted into two pairs of peaks at 159 eV (Bi $4f_{7/2}$) and 164 eV (Bi $4f_{5/2}$) corresponding to the binding energy of Bi^{3+} in V_2C/BVO.[32] Similarly for V_2C/Bi composite, the Bi 4f peaks correspond to oxidized surface (Bi^{3+}) of the nanoparticles.[48] The fitting results of the respective elements are listed in Table S1.†

Since the SSA of the catalyst plays a significant role in catalytic activity, we next measured the Brunauer–Emmett–Teller (BET) SSA of the samples by nitrogen absorption and desorption test. As depicted in Fig. S4,† the composite V_2C/BVO possesses a larger SSA (8.56 m^2 g^{-1}) and pore volume value (0.121 cm^3 g^{-1}) compared to V_2C/Bi and pristine V_2C. The larger pore volume and SSA confirmed that the 2D/2D composite with 2D/2D structure possesses an increased number of active sites for redox reactions.
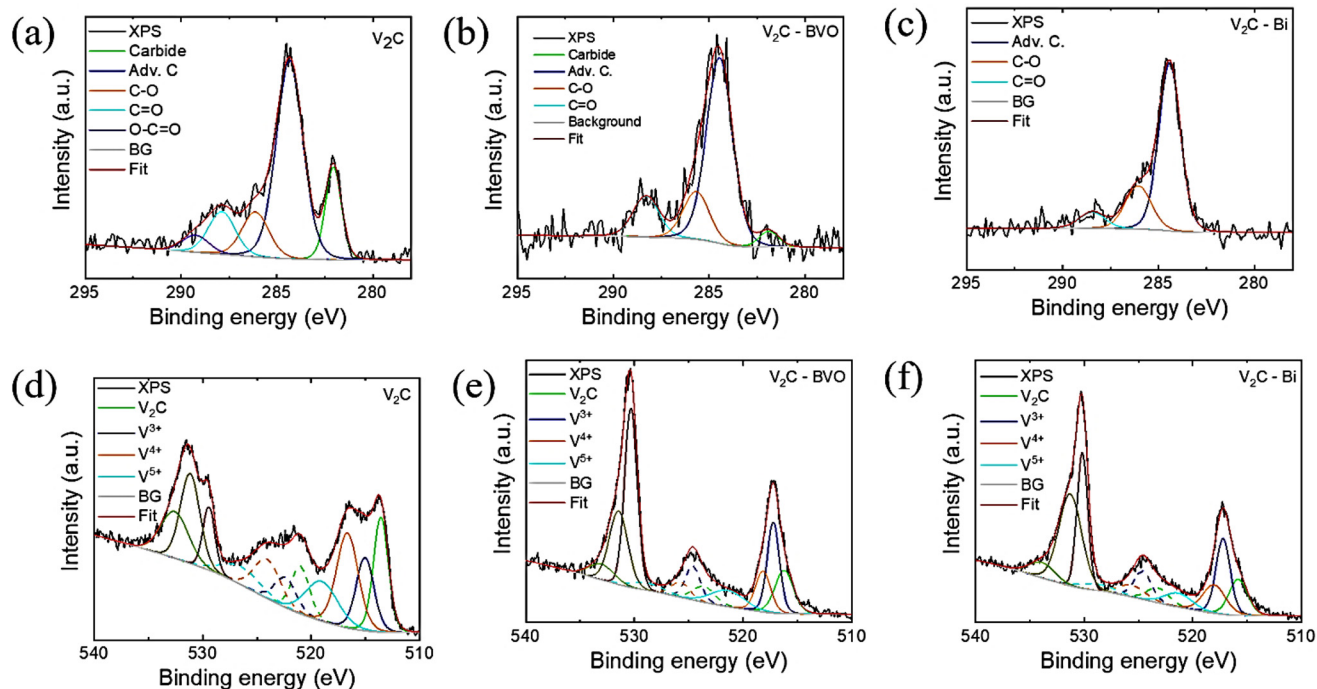
Fig. 3 High-resolution XPS spectra of C 1s in (a) V_2C, (b) V_2C/BVO, and (c) V_2C/Bi; high-resolution XPS spectra of V 2p in (d) V_2C, (e) V_2C/BVO, and (f) V_2C/Bi.

3.2. Catalytic HER activity

The HER activity of all the catalysts was measured by linear sweep voltammetry (LSV) in 0.5 M H_2SO_4 using three-electrode cells. The HER activity was compared to commercial Pt/C (20 wt%) and glassy carbon electrode (GC). As shown in Fig. 4a, the GC electrode displayed negligible HER activity which indicates that the observed activity is mainly due to the catalysts. As expected, the Pt/C (20 wt%) shows the highest catalytic activity with an overpotential of 68 mV at 10 mA cm^{-2} current density (Fig. 4b). In comparison, the V_2C/BVO (with an overpotential of 384 mV at 10 mA cm^{-2}) exhibited a much
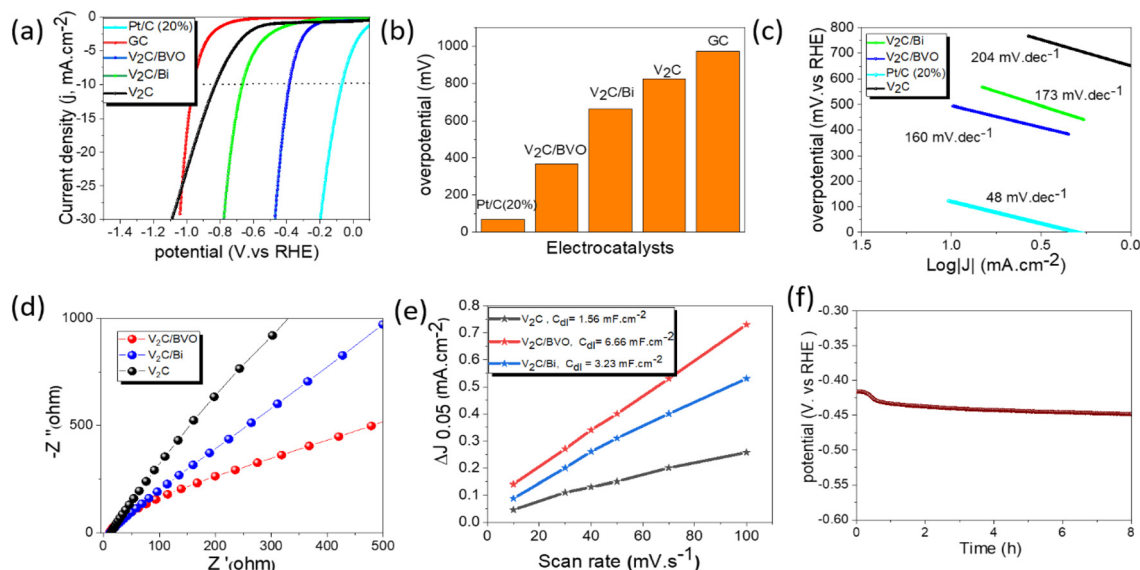

Fig. 4 Electrochemical measurements for hydrogen evolution in 0.5 M H_2SO_4 acidic medium: (a) LSV curves, (b) onset overpotential at j = 10 mA cm^{-2} of different electrocatalysts, (c) the corresponding Tafel plots, (d) EIS Nyquist plot of different catalysts, (e) capacitive Δj as a function of scan rates for different samples, and (f) the chronoamperometric measurement for V_2C/BVO at a constant current density of −10 mA cm^{-2}.

better HER performance than V_2C/Bi (663 mV) and V_2C (823 mV), indicating that the formed 2D/2D V_2C/BVO hybrid provided the active species for the HER. The overpotential (η_{10}) of the V_2C/BVO electrocatalyst corresponding to a current density of 10 mA cm^{-2} is further compared to these non-noble metal electrocatalysts in Table S2.† It should be noted that the V_2C/BVO catalyst needs lower overpotential compared to previously reported catalysts. Following this, we evaluated the Tafel slope which is often used to characterize the rate-limiting step of electrocatalytic reaction. The HER mechanism in acidic media is based on two possible reaction pathways namely: (a) Volmer–Heyrovsky and (b) Volmer–Tafel. HER starts with the Volmer reaction, where the hydronium protons acquire electrons on the surface of the electrode and generate an adsorbed hydrogen atom H_{ads} as an intermediate state ($H_3O^+ + e^- \rightarrow H_{ads} + H_2O$). Then, H_2 molecules are dominantly generated through one of two different reaction processes depending on the surface coverage of H_{ads}. If the coverage of H_{ads} is high, two H_{ads} combine to form H_2, so the Tafel reaction becomes the rate-determining step for the H_2 production ($H_{ads} + H_{ads} \rightarrow H_2$). In reverse, if the coverage of H_{ads} is low the Heyrovsky reaction becomes the rate-determining step, where a single H_{ads} atom attracts both a proton and an electron (e^-) to produce an H_2 molecule ($H_{ads} + e^- + H_3O^+ \rightarrow H_2 + H_2O$). When the Volmer step is the rate-limiting step, the Tafel slope reaches 120 mV dec^{-1}. Whereas the Tafel slope is reduced to 40 or 30 mV dec^{-1} when the Heyrovsky step or Tafel step is the rate-limiting step.[52,53] Fig. 4c presents the Tafel plots of all samples, where V_2C/BVO shows a smaller Tafel slope of 160 mV dec^{-1} than those of V_2C/Bi (173 mV dec^{-1}) and V_2C (204 mV dec^{-1}), revealing that the HER process of V_2C/BVO is controlled by the Volmer–Heyrovsky mechanism and the Volmer step is the rate-determining step.[54,55] As previously reported, under acidic conditions, the reaction between –O functional groups on the surface of MXenes and H^+ ions in H_2SO_4 aqueous solution promotes the current before the HER process, which explains the main reason for the high Tafel slope in the current study.[56,57] To further probe the origin of the enhanced HER performance of prepared electrocatalysts, the EIS measurement is a crucial method to investigate the interfacial properties and the charge-transfer resistance between the solution and the electrode. Meanwhile, the arc radius in the EIS Nyquist plots could be a credible method to estimate the charge transfer rate.[58] It was commonly believed that a smaller arc in the EIS Nyquist plot implied less charge migration resistance.[58–60] As displayed in Fig. 4d, V_2C/BVO composite displayed a smaller arc radius, indicating faster charge transfer at the electrode/electrolyte interface, leading to enhanced HER performance. The exchange current density (j_0) is another important parameter in the evaluation of HER activity, which is defined by the cathodic current density of the Tafel equation at the zero overpotential. The j_0 of all the catalysts was evaluated from the Tafel plot by extending to X-axis (Fig. S5†). The j_0 of the V_2C/BVO hybrid is estimated to be 16 µA cm^{-2} which is significantly higher than the V_2C/Bi (10 µA cm^{-2}) and V_2C (9 µA cm^{-2}). It is reflected that the inter-

facial electronic coupling could boost the electron transfer capability of V_2C/BVO hybrids for HER catalysis.[61] In addition, to better understand the intrinsic activity of the catalyst, we further evaluated the double-layer capacitance (C_{dl}) by a series of cyclic voltammetry (CV) measurements at different scan rates from 10 to 100 mV s^{-1} in the capacitive range of 0 to 0.1 V ($vs.$ RHE). As expected, the V_2C/BVO electrode exhibits a higher current than that of V_2C and V_2C/Bi as shown in Fig. S6.† It indicates more accessible active sites are created during hydrothermal synthesis of V_2C/BVO which is favourable for the enhanced HER activity. To calculate the double layer capacitance (C_{dl}), we first determined the capacitive density current average (Δj) using the formula $\Delta j = |j_c - j_a|/2$, where j_c represents the cathodic density current and j_a represents the anodic density current. At a potential of 0.05 V, we plotted Δj against various scan rates and determined the linear slope value, which corresponded to C_{dl}.[62] As shown in Fig. 4e, the C_{dl} of V_2C/BVO (6.66 mF cm^{-2}) was much larger than that of V_2C/Bi (3.23 mF cm^{-2}) and V_2C (1.56 mF cm^{-2}) which was attributed to the high SSA of the 2D/2D V_2C/BVO composite and is beneficial to the exposure of more accessible active sites for the HER and diffusion of electrocatalytic active species.[63,64] We can conclude that the $BiVO_4$ which is in $situ$ formed and uniformly coated on the V_2C layers provides additional active sites for HER reaction. Therefore, the actual active site responsible for the HER reaction in the V_2C/BVO composite is the interface between the V_2C and $BiVO_4$ layers, where synergistic effects may occur.

All the electrochemical measurements for HER reactions show that V_2C/BVO composite exhibits impressive electrocatalytic ability in acidic media compared to pure V_2C and V_2C/Bi composite. The outstanding electrocatalytic performance of the V_2C/BVO composite is supposed to be originating from; (i) a well-constructed 2D/2D (V_2C/BVO) structure which is beneficial to increase the SSA, which allows the exposure of numerous catalytic active sites and full penetration of electrolyte, (ii) the synergistic effect of V_2C and $BiVO_4$, and their intrinsic electrocatalytic response, and (iii) the high metallic conductivity of V_2C MXene sheets acts as a conductive material which facilitates electron transport. All these features confirm that the newly prepared composite (V_2C/BVO) in a facile hydrothermal way could be considered as a promising non-noble catalyst for HER application. HER efficiencies of as-prepared V_2C/BVO composite were also evaluated as electrocatalyst for HER in alkaline (1 M KOH, pH = 14) and neutral solution (1 M Na_2SO_4, pH = 7). Fig. S7a† shows that V_2C/BVO composite exhibits a high overpotential of 584 and 679 mV at a current density of 10 mA cm^{-2} in basic and neutral media, respectively. The results suggest that the HER reactions of V_2C/BVO under alkaline conditions are harder than in acidic solutions. This indicates the ability of the V_2C/BVO catalyst to adsorb hydrogen rather than accelerated water dissociation.

Long-term stability testing on V_2C/BVO was also carried out by a chronopotentiometry test. Fig. 4f shows low voltage increasing over 8 h at a constant current density (10 mA cm^{-2})

operation. Fig. S7(b and g)† shows the SEM, EDS, and XPS of the catalyst after the stability test. SEM and EDS elemental mapping images show that V_2C/BVO still has a multilayer structure without being damaged and the existence of all chemical composition as before electrolysis. As well, post-stability XPS measurements indicate the high structural stability of V_2C/BVO toward the HER process. Furthermore, we conducted the EIS analysis after stability as shown in Fig. S7h.† The Nyquist plots displayed that the arc radius of the V_2C/BVO composite after and before stability is mostly identical, revealing the same charge transfer capacity and, therefore, no considerable alteration of the electrical properties confirming the high stability of V_2C/BVO.

3.3. Evaluation of NRR performance

The Electrochemical NRR measurements were performed in a two-compartment cell (H-cell) as shown in Fig. S8.† The LSV curves of catalysts were compared under an N_2-saturated 0.1 M KOH electrolyte (Fig. 5a). It can be found that the current value of V_2C/Bi is higher than that of V_2C and V_2C/BVO at the same potential, suggesting its superior catalytic activity. The result further proves that the addition of the metal Bi effectively improved the catalytic performance of the V_2C. Linear sweep voltammetry (LSV) measurements of the V_2C/Bi composite were then performed in Ar- and N_2-saturated 0.1 M KOH aqueous under room temperature and atmospheric pressure (Fig. 5b). Obviously, the reduction of current density in the potential range of −0.4 V to −0.7 V of V_2C/Bi in N_2 is slightly lower than that of the Ar atmosphere, implying that NRR was

more favourable over HER in the measured potential window. Next, a CV test was performed between −1 V and 1.8 V vs. RHE in N_2-saturated KOH. Fig. S9a† shows 3 peaks at 0.45, 0, and −0.56 V vs. RHE. The anodic and cathodic signals at 0.45 and 0 V vs. RHE can be assigned to the surface reversible oxidation and subsequent reduction of the electrocatalyst. Specifically, these signals indicate the interconversion of species between Bi (0) and Bi $(OH)_3$ (or BiOOH) during the electrochemical reaction.[65] The broad cathodic peak that appears at −0.56 V is attributed to the reduction of Bi^{3+} to metallic Bi.[66,67] This observation is consistent with the XRD results, which showed the presence of a small amount of Bi_2O_3 in the V_2C/Bi composite. The complete reduction of Bi^{3+} to metallic Bi occurs during the first scan and subsequent scans may not show this cathodic peak due to the saturation of the surface with metallic Bi. After 3 consecutive cycles, the CV curves are almost identic, confirming the stability of the electrode before the NRR test. The electrochemical NRR performances of catalysts were further evaluated by chronoamperometry tests under potentials ranging from −0.3 to −0.7 V vs. RHE for 2 h in N_2-saturated KOH aqueous solution as shown in Fig. S9b–d.† It is clearly depicted that the current density improved with the increase of potential and remains almost stable during the two hours at different potentials, implying that both V_2C/Bi and V_2C/BVO composites exhibit good electrochemical stability during the NRR test. While for V_2C, at −0.5 V vs. RHE, the current density increased from the initial −0.13 mA cm^{-2} value to about −1.84 mA cm^{-2} after 2 h, indicating an in situ transformation during the electrocatalytic tests. It is possible
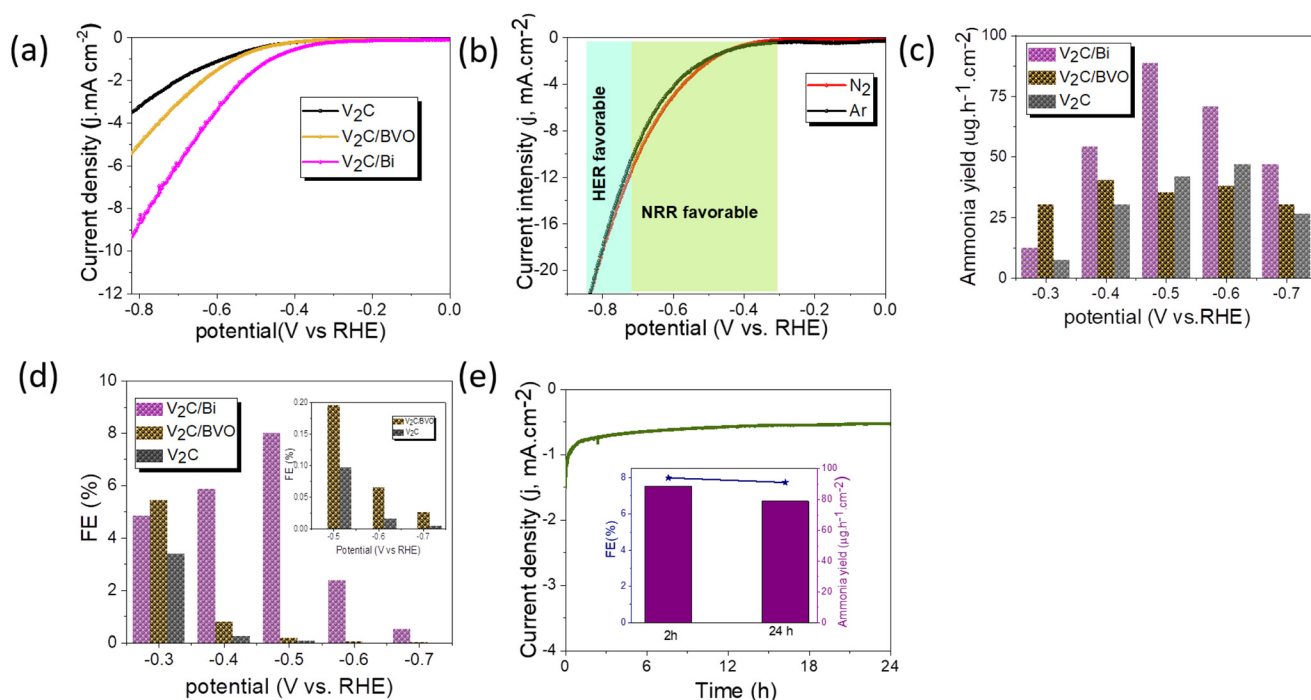

Fig. 5 (a) Comparison of LSV curves of GC electrode, V_2C, V_2C/BVO, and V_2C/Bi in N_2-saturated 0.1 M KOH with a scan rate of 10 mV s^{-1}, (b) LSV curves of V_2C/Bi in Ar/N_2-saturated KOH electrolyte with a scan rate of 10 mV s^{-1}, (c) corresponding NH_3 yields (d) corresponding FE, (e) chronoamperometric test of V_2C/Bi at −0.5 V for 24 h (insert: corresponding NH_3 yields and FE after stability test).

that the decrease in current density observed during the electrocatalytic experiment was due to the oxidation of V_2C and the formation of VO_x species. These oxide layers can act as passivating layers that hinder electron transfer between the V_2C and the electrolyte solution, leading to a decrease in current density over time. After electrolysis at a given potential, the generated ammonia was determined spectrophotometrically by Nessler's method. The NH_3 production and corresponding FE under different potentials are displayed in Fig. 5c and d. As clearly shown, the V_2C/Bi composite exhibits the highest NH_3 yield of 88.6 µg h^{-1} cm^{-2} and the highest faradaic efficiency (FE) of 8% at −0.5 V vs. RHE which are both higher than the values obtained for V_2C/BVO (NH_3 yield: 40.5 µg h^{-1} cm^{-2}, FE: 5.45%). For confirmation, the indophenol method (Fig. S10d–f†) was also used to measure the concentration of ammonia for V_2C/Bi at −0.5 V (V vs. RHE), and the result was 92 µg h^{-1} cm^{-2}, which is close to the value calculated from the Nessler's reagent method. This result confirms that both methods produce consistent values.

We compared the ammonia yield rates and the corresponding faradaic efficiencies of V_2C/Bi with those of the recently reported MXenes-based NRR catalysts. As listed in Table S3,† the ammonia yield produced over V_2C/Bi is significantly higher than that of all the listed catalysts. Furthermore, we evaluated the NRR performance of the pristine V_2C. Compared to V_2C/Bi, V_2C exhibits significantly lower NRR activity (NH_3 yield: 46.8 µg h^{-1} cm^{-2}, FE: 3.4%), implying that the Bi supported on V_2C should be the main active sites for NRR for V_2C/Bi. Obviously, the NH_3 yield, and FE decreased when the applied potentials shifted to more negative values, mainly due to the competitive adsorption between N_2 and H_2 on the electrode surface. Furthermore, no N_2H_4 could be detected after the electrocatalytic NRR at different potentials. This further confirms the outstanding selectivity of the V_2C/Bi catalyst. To confirm the electrochemical reduction of N_2 to NH_3 on V_2C/Bi, three controlled experiments were conducted: (i) the working electrode in electrolyte with continual Ar flow at −0.5 V for 2 h electrolysis; (ii) the working electrode with continual N_2 flow at open circuit potential (OCP) for 2 h elec-

trolysis; and (iii) bare glassy carbon electrode in electrolyte with continual N_2 flow at −0.5 V for 2 h electrolysis. As shown in Fig. S10,† very low current density and very low NH_3 and corresponding FE were detected for all those control experiments, suggesting that the produced NH_3 is derived from the electrochemical N_2 reduction catalyzed by the V_2C/Bi catalyst.

For electrocatalytic NRR, long-term catalytic stability is critical for the possible practical application. Fig. 5e shows a very steady current density over 24 h of continuous chronoamperometric test at −0.5 V, with a 90.5% retention of its initial NH_3 yield and almost unchanged FE after 24 h (inset Fig. 5e). Additionally, the SEM images and corresponding EDS elemental mapping (Fig. S11†) of the V_2C/Bi after stability revealed that the morphology and the chemical composition have no obvious changes compared to the fresh one, proving the robustness of the heterostructure for stable NRR performance. To further evaluate the long-term stability of V_2C/Bi catalyst, EIS analysis was recorded before and after 24 h of chronoamperometry analysis. Fig. S11e† indicates that the catalyst exhibits negligible deviation of the arc radius after stability which confirms its excellent long-term stability. Furthermore, the XPS spectra after NRR stability (Fig. S11f–h†) confirm that the V_2C/Bi well retains its initial chemical bonding state for V 2p and C 1s. The appearance of two new peaks with low intensity at 157.4 and 162.4 eV in the Bi 4f spectra indicates the presence of Bi^0. As discussed earlier, V_2C/Bi composite exhibits reversible redution at 0 V vs. RHE (Fig. S9a†) of bismuth nanoparticles. Thus, these nanoparticles were reduced during the long term experiment to metalic Bi. Subsequently when exposed to air/oxygen, their surface was again oxidized. All the above results unambiguously demonstrate V_2C/Bi to be a promising NRR catalyst for efficient NH_3 electro-synthesis. Generally, the NRR reaction process involves continuous proton–electron pairs interacting with N_2. As already proven HER is the main competitive reaction of the NRR. Therefore, increasing N_2 coverage on the electrocatalyst and suppressing the HER process during NRR is an effective strategy to increase the selectivity to NH_3. Hence, we study the HER activity of the V_2C/Bi nanocomposite and compare it with that of V_2C
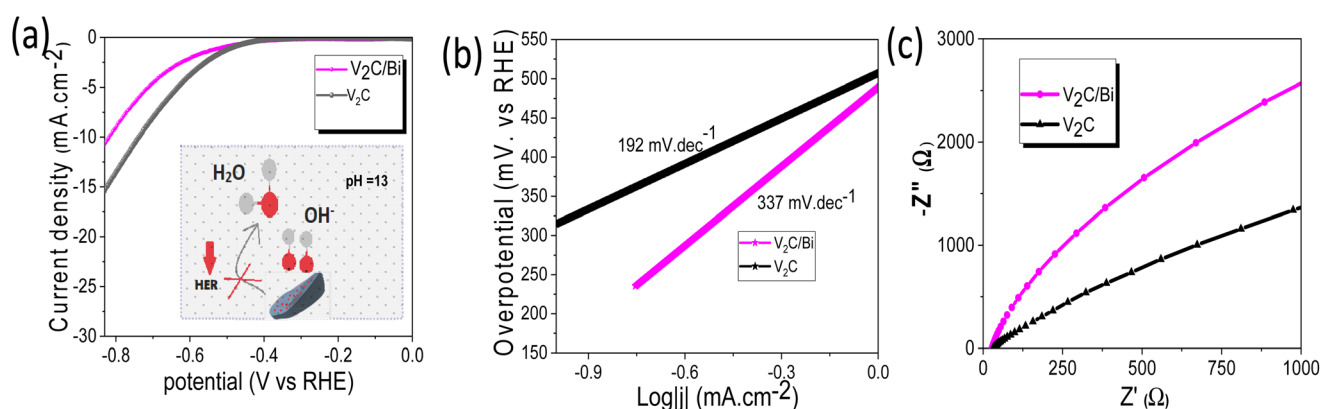

Fig. 6 (a) LSV of V_2C/Bi and V_2C in Ar saturated KOH (insert: the deactivation mechanism of the HER process over V_2C/Bi), (b) the corresponding Tafel plots analysis, and (c) EIS of V_2C and V_2C/Bi.

MXene. As shown in Fig. 6a, V_2C/Bi exhibited lower HER performance compared to V_2C. The Tafel slopes of the samples were then calculated. As demonstrated in Fig. 6b, the Tafel slopes of the V_2C/Bi composite were higher than that of the pristine V_2C MXene, indicating a less favourable kinetics process for HER over the V_2C/Bi electrode. In addition, the EIS measurement (Fig. 6c) shows that the arc radius of V_2C/Bi is significantly larger than that of V_2C, indicating low electron transfer in the composite and resulting in lower HER performance. This result confirms the negative effect of the Bi nanoparticles on HER, which, on the other hand, is highly beneficial for the improvement of NRR performance for gradually elevated ammonia yields. Thus, we proved that the HER process can be significantly repressed with Bi by inhibiting the adsorption of H on active sites. The same result has already been proven by previous researchers when studying the NRR activity of the Mo-doped V_2C system.[68] Theoretical calculations confirmed that $\Delta G_{N_2*} > \Delta G_{H^+*}$ on Mo-doped V_2C, which confirms the restriction of the HER reaction after doping of V_2C with Mo.

In this study, the V_2C/Bi heterojunction is produced by supporting the Bi-metal on O-terminated V_2C, indicating that V_2C can offer electrons that can be transported to Bi through the heterojunction interface (Fig. S12†). The electrons provided by V_2C are mainly accumulated at the V_2C/Bi interface. Such electron-rich interfaces facilitate the downshift of the p-band centre of interfacial Bi atoms,[69] which serve as the main active sites to promote the N_2 activation and hydrogenation while impeding the competing hydrogen evolution. This suggests the outstanding selectivity of V_2C/Bi for N_2-to-NH_3 conversion.

4. Experimental procedures

4.1 Synthesis of layered V_2C

Multilayered V_2C MXene powder was obtained by etching Al from V_2AlC powder according to a previous report.[70] Briefly, 6 g NaF was dissolved in 120 mL of deionized water, then 140 mL HCl solution (6 mol L^{-1}) was added to obtain the etching solution. After that, 6 g of as-received V_2AlC MAX phase powder was slowly added to the etching solutions in Teflon-lined stainless-steel autoclaves (500 mL). The Teflon bottle was kept in an oil bath with magnetic stirring at 90 °C for 5 days. After the end of the etching process, the dispersion was then centrifuged at 5000 rpm for 5 min to harvest the sediment, which was further centrifuged and washed with deionized (DI) water and ethanol six times to raise the pH of the supernatant to almost neutral (pH ~ 7). Finally, the solid product was collected and then placed in a vacuum freeze dryer at −50 °C for 24 h to remove the residual water and obtain a powder of V_2C MXene.

4.2. Synthesis of V_2C/BVO by hydrothermal method

The composite V_2C/BVO was synthesized through a facile hydrothermal method (Fig. 7). To do this, 100 mg of the prepared V_2C MXene powder was put in 40 mL of deionized water
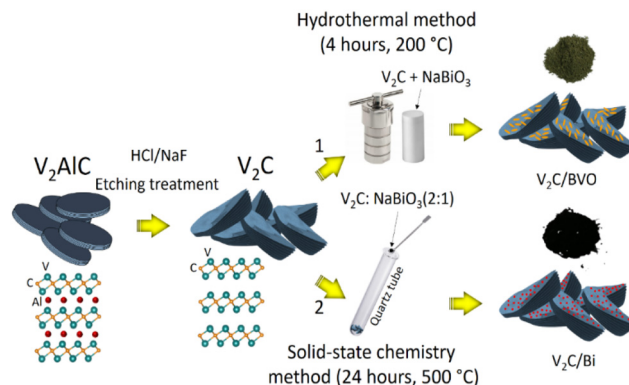

Fig. 7 A schematic illustration of the synthesis of composites V_2C/BVO and V_2C/Bi.

and ultrasonically dispersed for 30 minutes to obtain a uniform MXene suspension. Another solution was prepared by dissolving 100 mg $NaBiO_3$ in 25 mL of deionized water. Then, the $NaBiO_3$ aqueous solution was slowly added to the uniform MXene suspension. The mixed suspension was vigorously stirred for 30 minutes, then transferred to a 100 mL Teflon-lined autoclave for 4 h at 200 °C. The dark green precipitate was centrifuged and thoroughly washed with deionized water and absolute ethanol several times. The V_2C/BVO composite was finally obtained by drying it in a vacuum oven at 60 °C overnight.

4.3. Synthesis of V_2C/Bi by solid-state annealing technique

The composite V_2C/Bi was synthesized through a solid-state annealing method following the steps described in the previous report (Fig. 7).[71] In this process, the obtained V_2C MXene and $NaBiO_3$ were mixed and crushed for 20 minutes with an agate mortar. After uniformly mixing the two components, the mixture powder was inserted inside a quartz ampoule and then was vacuum sealed to a pressure of approximately 10^{-5} mbar using a vacuum pump. The vacuum sealing of the ampoule was required to prevent the mixture from moisture. Finally, the sealed ampoule including the mixture was placed in a furnace and heated at 500 °C for 24 h using a 5 °C min^{-1} heating and cooling rate. After annealing, the ampoule was removed from the furnace and cooled in the air. Then, it was opened, and the black precipitate was manually collected.

4.4. Characterization

X-ray diffraction (XRD) patterns of the synthesized materials were acquired on a Bruker D8 diffractometer operating at 40 kV with Cu Kα radiation (λ = 1.54056 Å). The diffraction patterns were collected between 5° and 60° with a step size of 0.02°. Scanning electron microscopy (SEM) was performed by a field-emission scanning electron microscope (FESEM, Tescan Lyra dual microscope) with attached energy-dispersive X-ray spectroscopy of a 20 mm^2 SDD detector (Oxford Instruments). Transmission electron microscopy (TEM, EFTEM Jeol 2200 FS microscope) equipped with energy dispersive spectrometry

(EDS) at an acceleration voltage of 200 kV. Raman spectra were performed by Raman spectrometer (Renishaw, England) in backscattering geometry with a CCD detector and a DPSS laser (532 nm, 50 mW) with an applied power of 0.5 mW. The samples were prepared by drop-casting a film on a nickel substrate, directly prior to the testing. X-ray photoelectron spectroscopy (XPS) analysis was recorded using a SPECS spectrometer equipped with an Al Kα X-ray source (1486.7 eV). The Brunauer–Emmett–Teller (BET) and pore size distribution of the samples were measured by a Micro-metrics ASAP 2020 apparatus at liquid nitrogen temperature.

4.5. Electrochemical measurements

4.5.1. Electrochemical HER measurements. All electrochemical measurements were carried out in a three-electrode system and a PGSTAT 204 (Utrecht, Netherlands, NOVA Version 2.1.4) electrochemical workstation at room temperature using Ag/AgCl as the reference electrode, carbon rod as the counter electrode, and the glassy carbon electrode as a working electrode. Initially, prior to the electrochemical measurements, the glassy carbon electrode (GC) was polished with an alumina suspension and then subjected to ultrasonic cleaning in double distilled water for 2 minutes. The working electrode was prepared as follows: 2 mg sample, 20 μL of Nafion solution (5 wt%), 100 μL of ethanol, and 300 μL DI water were dispersed by sonication for 30 minutes. A dispersed ink of 10 μL was coated onto the surface of a working electrode using the drop-casting method and dried under a vacuum. The Ag/AgCl reference electrode was calibrated with respect to a reversible hydrogen electrode (RHE) according to the Nernst equation:

$$E_{RHE} = E_{Ag/AgCl} + 0.197 + 0.059 \text{ pH}$$

Linear sweep voltammetry (LSV) was performed in 0.5 M H_2SO_4 with a sweep rate of 5 mV s^{-1}. The Tafel slope of the catalyst can be calculated by the formula $\eta = a + b \log|j|$ (η, a, b, and j are standing for overpotential, Tafel constant, Tafel slope, and current density, respectively). The overpotential for HER was calculated using the following equation $\eta = 0 - E$ (vs. RHE (V)). Electrochemical impedance spectroscopy (EIS) was recorded by applying an AC potential amplitude of 10 mV within the frequency range from 0.1–1000 Hz. The double-layer capacitances were obtained through cyclic voltammetry (CV) with various scan rates in the voltage range of 0–0.1 V vs. RHE.

4.5.2. Electrochemical NRR measurements. Electrochemical measurements were performed with an Autolab PGSTAT 204 (Metroohm, Switzerland) in a two-compartment cell (H-cell) electrocatalytic system separated by a proton-exchange membrane (Nafion 211) at room temperature and atmospheric pressure. A platinum plate, Ag/AgCl/saturated KCl, and glassy carbon (effective area: 0.158 cm^2) were used as a counter electrode, reference electrode, and working electrode, respectively. The working electrode was polished and prepared following the above-mentioned steps. All potentials in this work were converted to the reversible hydrogen electrode (RHE) using the Nernst equation ($E_{RHE} = E_{Ag/AgCl} + 0.197 + 0.059$ pH). Before

performing the NRR test, a Nafion membrane was pretreated in H_2O_2 (5 wt%) aqueous solution at 80 °C and then in ultra-pure water at 80 °C each for 1 hour. For NRR experiments, 0.1 M KOH (50 mL in each cell compartment) was purged with N_2 (99.99%) using a constant flow of 20 mL min^{-1} during the whole electrolytic process, and a 40 mL acid trap (0.1 M H_2SO_4) was connected to both compartments. The chronoamperometry tests were conducted at a series of applied potentials (−0.3, −0.4, −0.5, −0.6, and −0.7 V vs. RHE) for 2 hours in ambient conditions. The LSV curves were collected in 0.1 M KOH aqueous solution saturated with Ar or N_2, at a sweep rate of 100 mV s^{-1}. A specific amount of ammonia (NH_3) produced in the acid trap was measured by HI83300 multi-parameter photometer (Hanna Instruments, Woonsocket, Rhode Island, USA). The ASTM D1426 Nessler method which has been noted in the previous report,[26] was adopted to determine the concentration of produced NH_3. Briefly, a cuvette filled with 10 mL of unreacted sample was placed in the photometer to obtain the background signal. Subsequently, four drops of ammonia low-range reagent A and ammonia low-range reagent B were added to the sample, then mixed thoroughly, and measured the absorbance of the reacted sample was at 420 nm.

The ammonia formation rate was calculated according to eqn (1):

$$NH_3 = \frac{C_{NH_3} \times V}{t \times A} \tag{1}$$

where C_{NH_3} is the measured NH_3 concentration, V is the volume of either the cathode or the acid trapped, t is the reduction reaction time and A is the area of the working electrode (0.158 cm^2).

The faradaic efficiency was calculated based on eqn (2):

$$FE = \frac{3F \times C_{NH_3} \times V}{MW_{NH_3} \times Q} \% \tag{2}$$

where F is the Faraday constant, MW_{NH_3} is the molecular weight of ammonia (17 g mol^{-1}), Q is the total charge of the electrode, and C_{NH_3} and V are as above explanations.

The amount of Hydrazine (N_2H_4) after the electrolysis reaction was detected by the D1385 method.[26] For determination of the generated hydrazine, 10 mL of the electrolyte after the NRR test was taken out and twelve drops of hydrazine reagent were subsequently added. The absorbance was measured at a wavelength of 466 nm, after 12 minutes.

5. Conclusions

Two nanocomposites consisting of 2D/2D V_2C/BVO and 2D/0D V_2C/Bi NPs were successfully prepared and applied for electrocatalytic HER and NRR. The V_2C/BVO composite has been synthesized via a facile hydrothermal method and applied as the catalyst electrode for HER in acidic conditions. Compared to pristine V_2C, the HER activity of V_2C/BVO has been greatly increased due to the strong interfacial interactions between BVO sheets and V_2C MXene nanosheets. This 2D/2D structure

provided sufficient active sites and ensured favorable electrochemical kinetics, improving the HER activity. Furthermore, the optimized composite showed excellent long-term stability over 8 h in acidic media at the current density of 10 mA cm^{-2}. Also, V_2C/Bi was proven to be a highly efficient NRR electrocatalyst, achieving a FE and NH_3 yield of 8% and 88.6 μg cm^{-2} h^{-1}, respectively. The obtained values are among the highest NRR selectivity for MXenes-based NRR catalysts. We also proved that impeding the competing HER by doping V_2C with p block metal (Bi) is an interesting strategy to achieve high N_2-to-NH_3 conversion.

This work provides inexpensive strategies for fabricating novel V_2C-based catalysts and may shed some light on energy-related applications.

Conflicts of interest

The authors declare no competing financial interest.

Acknowledgements

References

1 J. Zhu, L. Hu, P. Zhao, L. Y. S. Lee and K.-Y. Wong, *Chem. Rev.*, 2020, **120**, 851–918.

2 G. Zhao, K. Rui, S. X. Dou and W. Sun, *Adv. Funct. Mater.*, 2018, **28**, 1803291.

3 S. L. Foster, S. I. P. Bakovic, R. D. Duda, S. Maheshwari, R. D. Milton, S. D. Minteer, M. J. Janik, J. N. Renner and L. F. Greenlee, *Nat. Catal.*, 2018, **1**, 490–500.

4 L. Zhang, K. Doyle-Davis and X. Sun, *Energy Environ. Sci.*, 2019, **12**, 492–517.

5 H. Liu, L. Syama, L. Zhang, C. Lee, C. Liu, Z. Dai and Q. Yan, *SusMat*, 2021, **1**, 482–505.

6 M. Naguib, M. Kurtoglu, V. Presser, J. Lu, J. Niu, M. Heon, L. Hultman, Y. Gogotsi and M. W. Barsoum, *Adv. Mater.*, 2011, **23**, 4248–4253.

7 D. A. Kuznetsov, Z. Chen, P. V. Kumar, A. Tsoukalou, A. Kierzkowska, P. M. Abdala, O. V. Safonova, A. Fedorov and C. R. Müller, *J. Am. Chem. Soc.*, 2019, **141**, 17809–17816.

8 A. Liu, X. Liang, X. Ren, W. Guan, M. Gao, Y. Yang, Q. Yang, L. Gao, Y. Li and T. Ma, *Adv. Funct. Mater.*, 2020, **30**, 2003437.

9 J. Zhang, Y. Zhao, X. Guo, C. Chen, C.-L. Dong, R.-S. Liu, C.-P. Han, Y. Li, Y. Gogotsi and G. Wang, *Nat. Catal.*, 2018, **1**, 985–992.

10 X. Wu, Z. Wang, M. Yu, L. Xiu and J. Qiu, *Adv. Mater.*, 2017, **29**, 1607017.

11 Z. W. Seh, K. D. Fredrickson, B. Anasori, J. Kibsgaard, A. L. Strickler, M. R. Lukatskaya, Y. Gogotsi, T. F. Jaramillo and A. Vojvodic, *ACS Energy Lett.*, 2016, **1**, 589–594.

12 J. Zhao, L. Zhang, X.-Y. Xie, X. Li, Y. Ma, Q. Liu, W.-H. Fang, X. Shi, G. Cui and X. Sun, *J. Mater. Chem. A*, 2018, **6**, 24031–24035.

13 Y. Luo, G.-F. Chen, L. Ding, X. Chen, L.-X. Ding and H. Wang, *Joule*, 2019, **3**, 279–289.

14 S. Li, P. Tuo, J. Xie, X. Zhang, J. Xu, J. Bao, B. Pan and Y. Xie, *Nano Energy*, 2018, **47**, 512–518.

15 L. Li, X. Wang, H. Guo, G. Yao, H. Yu, Z. Tian, B. Li and L. Chen, *Small Methods*, 2019, **3**, 1900337.

16 A. D. Handoko, K. D. Fredrickson, B. Anasori, K. W. Convey, L. R. Johnson, Y. Gogotsi, A. Vojvodic and Z. W. Seh, *ACS Appl. Energy Mater.*, 2018, **1**, 173–180.

17 L. R. Johnson, S. Sridhar, L. Zhang, K. D. Fredrickson, A. S. Raman, J. Jang, C. Leach, A. Padmanabhan, C. C. Price, N. C. Frey, A. Raizada, V. Rajaraman, S. A. Saiprasad, X. Tang and A. Vojvodic, *ACS Catal.*, 2020, **10**, 253–264.

18 C. Ling, L. Shi, Y. Ouyang, Q. Chen and J. Wang, *Adv. Sci.*, 2016, **3**, 1600180.

19 W. Kong, F. Gong, Q. Zhou, G. Yu, L. Ji, X. Sun, A. M. Asiri, T. Wang, Y. Luo and Y. Xu, *J. Mater. Chem. A*, 2019, **7**, 18823–18827.

20 J. Liu, Y. Liu, D. Xu, Y. Zhu, W. Peng, Y. Li, F. Zhang and X. Fan, *Appl. Catal., B*, 2019, **241**, 89–94.

21 K. Li, T. Jiao, R. Xing, G. Zou, Q. Zhao, J. Zhou, L. Zhang and Q. Peng, *Green Energy Environ.*, 2018, **3**, 147–155.

22 P. Li, J. Zhu, A. D. Handoko, R. Zhang, H. Wang, D. Legut, X. Wen, Z. Fu, Z. W. Seh and Q. Zhang, *J. Mater. Chem. A*, 2018, **6**, 4271–4278.

23 T. A. Shifa, F. Wang, Y. Liu and J. He, *Adv. Mater.*, 2019, **31**, 1804828.

24 R. Zhang, L. Ji, W. Kong, H. Wang, R. Zhao, H. Chen, T. Li, B. Li, Y. Luo and X. Sun, *Chem. Commun.*, 2019, **55**, 5263–5266.

25 L. Li, C. Tang, B. Xia, H. Jin, Y. Zheng and S.-Z. Qiao, *ACS Catal.*, 2019, **9**, 2902–2908.

26 N. Antonatos, J. D. Elliott, V. Mazánek, P. Marvan, P. Carbone, W. Geng, Y. Jing and Z. Sofer, *J. Mater. Chem. A*, 2022, **10**, 11904–11916.

27 S. Mourdikoudis, N. Antonatos, V. Mazánek, I. Marek and Z. Sofer, *Inorg. Chem.*, 2022, **61**, 5524–5538.

28 A. Liu, X. Liang, H. Zhu, X. Ren, L. Gao, M. Gao, Y. Yang, G. Li and T. Ma, *ChemCatChem*, 2022, **14**, e202101683.

29 J. Greeley, T. F. Jaramillo, J. Bonde, I. Chorkendorff and J. K. Nørskov, *Nat. Mater.*, 2006, **5**, 909–913.

30 H.-x. Pan, L.-p. Feng, W. Zeng, Q.-c. Zhang, X.-d. Zhang and Z.-t. Liu, *Inorg. Chem.*, 2019, **58**, 13195–13202.

31 Z. Wu, J. Mei, Q. Liu, S. Wang, W. Li, S. Xing, J. Bai, J. Yang, W. Luo, O. Guselnikova, A. P. O'Mullane, Y. Gu, Y. Yamauchi, T. Liao and Z. Sun, *J. Mater. Chem. A*, 2022, **10**, 808–817.

32   Y. Li, Y. Liu, D. Xing, J. Wang, L. Zheng, Z. Wang, P. Wang, Z. Zheng, H. Cheng, Y. Dai and B. Huang, *Appl. Catal., B*, 2021, **285**, 119855.

33   Y. Guan, S. Jiang, Y. Cong, J. Wang, Z. Dong, Q. Zhang, G. Yuan, Y. Li and X. Li, *2D Mater.*, 2020, **7**, 025010.

34   S. A. Zahra, B. Anasori, M. Z. Iqbal, F. Ravaux, M. Al Tarawneh and S. Rizwan, *APL Mater.*, 2022, **10**, 060901.

35   H. Chand, M. Sharma and V. Krishnan, *Sep. Purif. Technol.*, 2022, **292**, 121032.

36   G. Zou, Z. Zhang, J. Guo, B. Liu, Q. Zhang, C. Fernandez and Q. Peng, *ACS Appl. Mater. Interfaces*, 2016, **8**, 22280–22286.

37   S. Dadashi, H. Delavari and R. Poursalehi, *Procedia Mater. Sci.*, 2015, **11**, 679–683.

38   W. Lv, G. Wu, X. Li, J. Li and Z. Li, *Energy Storage Mater.*, 2022, **46**, 138–146.

39   D. Sha, C. Lu, W. He, J. Ding, H. Zhang, Z. Bao, X. Cao, J. Fan, Y. Dou, L. Pan and Z. Sun, *ACS Nano*, 2022, **16**, 2711–2720.

40   L. Qin, S. Xu, Y. Liu, S. Zhu, L. Hou and C. Yuan, *Chin. Chem. Lett.*, 2020, **31**, 1030–1033.

41   A. Champagne, L. Shi, T. Ouisse, B. Hackens and J.-C. Charlier, *Phys. Rev. B*, 2018, **97**, 115439.

42   M. V. Malashchonak, E. A. Streltsov, D. A. Kuliomin, A. I. Kulak and A. V. Mazanik, *Mater. Chem. Phys.*, 2017, **201**, 189–193.

43   M. Gotić, S. Musić, M. Ivanda, M. Šoufek and S. Popović, *J. Mol. Struct.*, 2005, **744–747**, 535–540.

44   S. Onari, M. Miura and K. Matsuishi, *Appl. Surf. Sci.*, 2002, **197–198**, 615–618.

45   Q. Su, C. K. Huang, Y. Wang, Y. C. Fan, B. A. Lu, W. Lan, Y. Y. Wang and X. Q. Liu, *J. Alloys Compd.*, 2009, **475**, 518–523.

46   Y. Wang, S. Wang, N. Dong, W. Kang, K. Li and Z. Nie, *Anal. Chem.*, 2020, **92**, 4623–4629.

47   P. Subramanyam, T. Khan, G. Neeraja Sinha, D. Suryakala and C. Subrahmanyam, *Int. J. Hydrogen Energy*, 2020, **45**, 7779–7787.

48   W. Hong, A. Wang, L. Li, T. Qiu, J. Li, Y. Jiang, G. Zou, H. Peng, H. Hou and X. Ji, *Adv. Funct. Mater.*, 2021, **31**, 2000756.

49   Y. Guo, T. Wang, Q. Yang, X. Li, H. Li, Y. Wang, T. Jiao, Z. Huang, B. Dong, W. Zhang, J. Fan and C. Zhi, *ACS Nano*, 2020, **14**, 9089–9097.

50   H. Yuan, Y. Jin, X. Chen, J. Lan, Y. Yu and X. Yang, *ACS Sustainable Chem. Eng.*, 2019, **7**, 6033–6042.

51   T. Wu, C. Zhang, H. Hou, P. Ge, G. Zou, W. Xu, S. Li, Z. Huang, T. Guo, M. Jing and X. Ji, *Adv. Funct. Mater.*, 2018, **28**, 1705744.

52   Z. W. Seh, J. Kibsgaard, C. F. Dickens, I. Chorkendorff, J. K. Nørskov and T. F. Jaramillo, *Science*, 2017, **355**, eaad4998.

53   J. Ding, H. Yang, S. Zhang, Q. Liu, H. Cao, J. Luo and X. Liu, *Small*, 2022, **18**, 2204524.

54   T. Wei, W. Liu, S. Zhang, Q. Liu, J. Luo and X. Liu, *Chem. Commun.*, 2023, **59**, 442–445.

55   H. Chen, S. Zhang, Q. Liu, P. Yu, J. Luo, G. Hu and X. Liu, *Inorg. Chem. Commun.*, 2022, **146**, 110170.

56   Y. Tan, Z. Zhu, X. Zhang, J. Zhang, Y. Zhou, H. Li, H. Qin, Y. Bo and Z. Pan, *Int. J. Hydrogen Energy*, 2021, **46**, 1955–1966.

57   M. Hu, Z. Li, T. Hu, S. Zhu, C. Zhang and X. Wang, *ACS Nano*, 2016, **10**, 11344–11350.

58   B. Shao, Z. Liu, G. Zeng, Z. Wu, Y. Liu, M. Cheng, M. Chen, Y. Liu, W. Zhang and H. Feng, *ACS Sustainable Chem. Eng.*, 2018, **6**, 16424–16436.

59   B. Shao, J. Wang, Z. Liu, G. Zeng, L. Tang, Q. Liang, Q. He, T. Wu, Y. Liu and X. Yuan, *J. Mater. Chem. A*, 2020, **8**, 5171–5185.

60   Y. Bai, H. Bai, Z. Fang, X. Li, W. Fan and W. Shi, *Chem. Commun.*, 2021, **57**, 10568–10571.

61   L. Li, D. Yu, P. Li, H. Huang, D. Xie, C.-C. Lin, F. Hu, H.-Y. Chen and S. Peng, *Energy Environ. Sci.*, 2021, **14**, 6419–6427.

62   Y. Li and C. Zhao, *ACS Catal.*, 2017, **7**, 2535–2541.

63   G. Meng, H. Cao, T. Wei, Q. Liu, J. Fu, S. Zhang, J. Luo and X. Liu, *Chem. Commun.*, 2022, **58**, 11839–11842.

64   D. Qi, F. Lv, T. Wei, M. Jin, G. Meng, S. Zhang, Q. Liu, W. Liu, D. Ma, M. S. Hamdy, J. Luo and X. Liu, *Nano Res. Energy*, 2022, **1**, e9120022.

65   W. Zheng, Y. Li, C. S. Tsang, P. K. So and L. Yoon Suk Lee, *iScience*, 2021, **24**, 102342.

66   Z. Fang, P. Wu, Y. Qian and G. Yu, *Angew. Chem., Int. Ed.*, 2021, **60**, 4275–4281.

67   J. Wu, Y. Miao, X. Liang, Z. Yang, Y. Yang and R. Ouyang, *Electroanalysis*, 2014, **26**, 856–863.

68   Y. Cao, Y. Tan, X. T. Zhu, H.-L. Li, Y.-Q. Zhao and Y. Xu, *Phys. E*, 2021, **134**, 114875.

69   X. Li, Y. Luo, Q. Li, Y. Guo and K. Chu, *J. Mater. Chem. A*, 2021, **9**, 15955–15962.

70   M. Wu, Y. He, L. Wang, Q. Xia and A. Zhou, *J. Adv. Ceram.*, 2020, **9**, 749–758.

71   P. K. Singh, S. K. Sharma, S. K. Tripathi and D. K. Dwivedi, *Results Phys.*, 2019, **12**, 223–236.